



CHALMERS

Chalmers Publication Library

Large Eddy Simulation of the Flow around one Single-Stacked Container Freight Wagon

This document has been downloaded from Chalmers Publication Library (CPL). It is the author's version of a work that was accepted for publication in:

in J. Pombo, (Editor), "Proceedings of the First International Conference on Railway Technology: Research, Development and Maintenance", Civil-Comp Press, Stirlingshire, UK, Paper 162, 2012. doi:10.4203/ccp.98.162 (ISSN: 1759-3433)

Citation for the published paper:

Östh, J. ; Krajnovic, S. (2012) "Large Eddy Simulation of the Flow around one Single-Stacked Container Freight Wagon". in J. Pombo, (Editor), "Proceedings of the First International Conference on Railway Technology: Research, Development and Maintenance", Civil-Comp Press, Stirlingshire, UK, Paper 162, 2012.
doi:10.4203/ccp.98.162

Downloaded from: <http://publications.lib.chalmers.se/publication/156987>

Notice: Changes introduced as a result of publishing processes such as copy-editing and formatting may not be reflected in this document. For a definitive version of this work, please refer to the published source. Please note that access to the published version might require a subscription.

Chalmers Publication Library (CPL) offers the possibility of retrieving research publications produced at Chalmers University of Technology. It covers all types of publications: articles, dissertations, licentiate theses, masters theses, conference papers, reports etc. Since 2006 it is the official tool for Chalmers official publication statistics. To ensure that Chalmers research results are disseminated as widely as possible, an Open Access Policy has been adopted. The CPL service is administrated and maintained by Chalmers Library.

(article starts on next page)

Abstract

In this work a time-dependent numerical simulation of the flow around a single standing container wagon model is presented. The model consists of a 11.8 m long container placed on the wagon. The model includes some geometrical details such as wheels and other undercarriage roughness. The Reynolds number in the study is 10^5 based on the width of the container. The simulation method used is the Large Eddy Simulation technique. The forces and the flow field are averaged in time and the results thereof are presented in the paper.

Keywords: Aerodynamics, Freight train, CFD, Large Eddy Simulation.

1 Introduction

The sum of the resistive forces acting on trains in the direction of travel is usually expressed as [1, 2, 3]:

$$F = A + B \times V + C \times V^2 \quad (1)$$

Here, it is assumed that the train does not accelerate and that it travels on flat ground and that the railway is straight. Otherwise, terms for the forces needed to overcome the resistance of acceleration, the gravitational force and mechanical curving resistance have to be included in Eq. 1. The term A on the right hand side contains mechanical resistances that are constant with respect to the speed of train, V , but dependent on the mass of the train. The second term contains resistances that are considered to be linearly proportional to the speed. The last term contains the aerodynamic resistance of the train which is proportional to the square of the speed. The coefficients in Eq. 1 are highly dependent on each specific train type under consideration and must be determined individually for each specific train [4, 5, 3]. However, many national

railways has developed empirical equations that can be used to estimate the resistance of a generic train. See Ref. [3] for a review of empirical equations used to estimate resistances of trains. A freight train normally consists of a large amount of wagons of different sizes, shapes and purposes. For a freight train the coefficient C in Eq. 1 is the sum of the contribution to the aerodynamic drag from the locomotive and all wagons in the train. The size of the contribution to C from each wagon depends on the position of the wagon in the train [6].

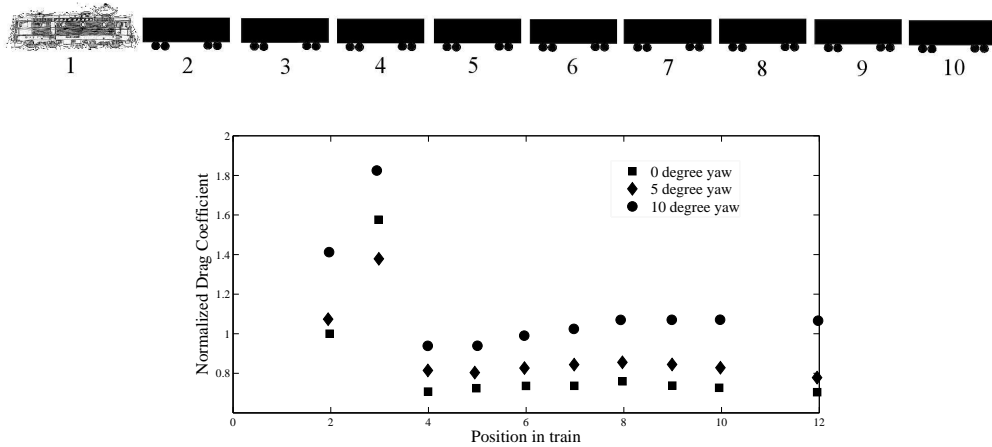


Figure 1: The top figure shows an arbitrary container freight train with a locomotive and 10 single stack wagons. The bottom figure shows the drag coefficient (y-axis) for a closed top gondola-type freight wagon depending on the position in the train (x-axis). All the values are normalized with the value of the drag coefficient of the wagon in the second position at zero yaw angle. The results are redrawn from the full-scale experimental study reported in Ref. [6].

Shown in Fig. 1 is the drag coefficient of a closed top gondola-type of freight wagon depending on the position in the train. Results are shown for 0, 5 and 10 degrees of yaw angle. It is seen that after the initial 3-4 wagons, the drag coefficient will reach some steady value that is some 20-50% less than the drag coefficient of the second wagon. The contribution to the total drag of the entire train from the locomotive will in turn be higher than the drag of the second wagon due to the contribution from the stagnation pressure of the air on the front of the locomotive. The majority of all the wagons in a freight train will experience an aerodynamic drag force slightly lower than that experienced by the first wagon in the train.

In the literature there are some experimental wind tunnel studies on different types of freight wagons reported. Wind tunnel simulations were made in Ref. [7] on 1:10 scale wagons. The objective of the study was to determine how a "typical" wagon in a train could be simulated in the wind tunnel. With "typical" means that the wagon should not experience effects in the measured flow quantities from the front or the rear

of the train. In the study it was found that for a wagon not to experience effects in the measured drag coefficient from the locomotive and or the end of the train one and a half dummy wagon was needed ahead of the wagon being studied. One half dummy wagon was needed downstream. In Ref. [8] measurements were done in wind tunnel on two open top rail type wagons. It was found that by dividing the cargo spacing into smaller subspaces the drag of each wagon was reduced when the train is operating with empty wagons. The lateral stability of a single double stacked container wagon subjected to crosswind was studied in Ref. [9]. The Reynolds number dependence of the aerodynamic drag force when the wagon was subjected to a wind of zero yaw angle was studied as well. It was found that for a Reynolds number larger than $\approx 0.8 \times 10^5$ based on the height from the ground of the double stacked wagon the measured drag coefficient showed little dependence on the Reynolds number for zero yaw.

The numerical simulation of the unsteady flow around a simplified freight wagon subjected to a crosswind at 90° yaw angle was reported in Ref. [10]. LES with the standard Smagorinsky model and $C_S = 0.1$ was used in the simulation and the Reynolds number was 3×10^5 based on the height of the freight wagon from the ground and the crosswind speed. The study reported in [10] is the only numerical study using unsteady simulation techniques to simulate the flow around any freight wagon model known to the authors of the present study.

The objective of the present study is to explore the flow around a single stack container freight wagon at 0° yaw angle. The method used to simulate the unsteady flow numerically is LES with standard Smagorinsky model. This method is the same as has been used in studies of flows around simplified train models in Refs. [11, 12, 13, 14, 10]. Due to the computational cost of the simulation and the complexity of the flow, only one wagon is considered in the present study. It remains to future studies to simulate the flow around a "typical" wagon in a train with wagons ahead and downstream of it. In Section 2 the geometry of simplified freight wagon model is described. In Section 3 the governing equations and the employed numerical technique to solve these is presented. In Section 4 the numerical accuracy in the simulation is evaluated. In Section 5 the results from the simulation are presented. In Section 6 the flow around the wagon is discussed and the paper is concluded in Section 7.

2 Description of the freight wagon model

The freight wagon model used in the present work is presented in Fig. 2. The model represents a single-stacked container freight wagon. The width of the container is $W = 2.354$ m and the length of the container is $5W$. In Fig. 2b a view of the front of the model is shown including some dimensions of the model. The total height of the model from the ground to the roof of the container is $1.6W$. The width between the inner edges of the wheels is $0.63W$ corresponding to the Normal Gauge of the width between the rails. The height from the ground to the container is $0.56W$. The

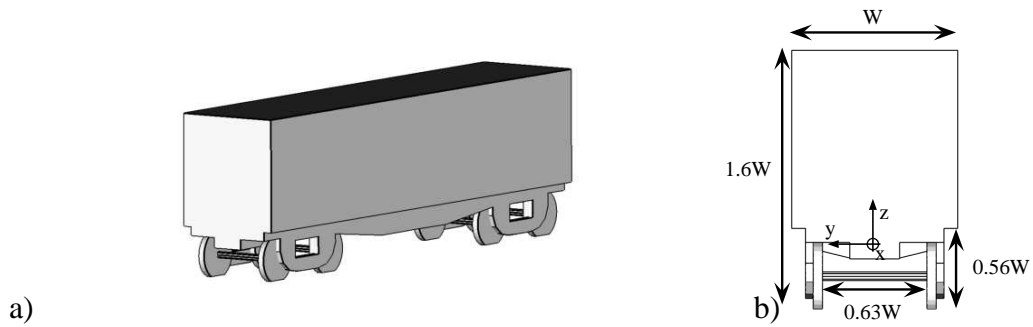


Figure 2: The container wagon model used in the present work. The model is simplified and details such as waffles on the container are smoothed. The model retains the main geometrical features of a real container wagon such as wheels and some undercarriage complexities.

coordinate system used in the present work is located on the front of the wagon as shown in Fig. 2b. The x-axis corresponds to the axis parallel but opposite to the direction of travel of the wagon. This direction is called the streamwise direction. The z-axis corresponds to the axis parallel with the direction of action of the gravitational force but in opposite direction to it. This axis is denoted the transversal direction to the flow. The y-axis is the axis perpendicular to both the x and z-axis and corresponds to the spanwise direction of the flow.

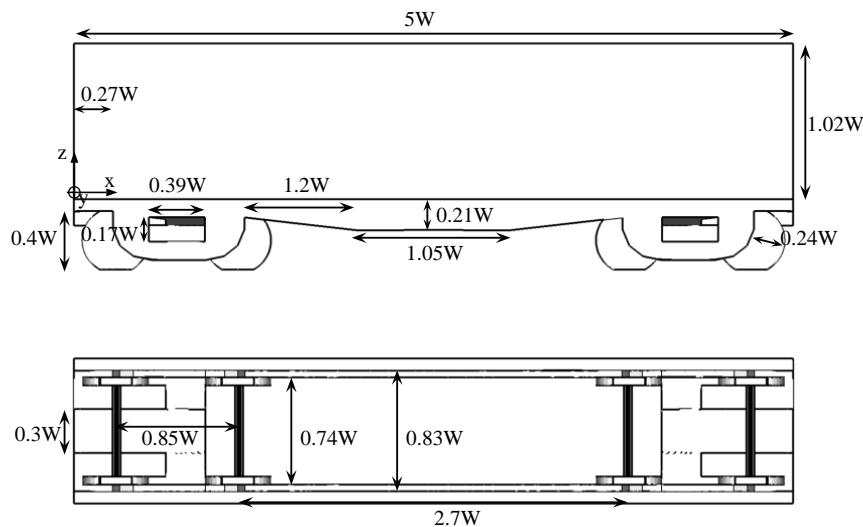


Figure 3: Details of the geometry.

In Figs. 3 the freight wagon model is shown from a side view (top) and view from below (bottom), respectively. The radius of the wheels is $0.24 W$. The wheels are cut at the bottom corresponding to 28° in order to simplify construction of the computation grid at the intersection of the wheels and the ground plane.

3 Numerical set-up

3.1 Governing Equations

The equations governing the air flowing around the wagon are the incompressible Navier-Stokes equations. By applying a spatial filter to these with the aim of removing the smallest isotropic and dissipative scales in the flow the incompressible filtered continuity and momentum equations are obtained:

$$\frac{\partial \bar{u}_i}{\partial x_i} = 0. \quad (2)$$

$$\frac{\partial \bar{u}_i}{\partial t} + \frac{\partial}{\partial x_j} (\bar{u}_i \bar{u}_j) = -\frac{1}{\rho} \frac{\partial \bar{p}}{\partial x_i} + \nu \frac{\partial^2 \bar{u}_i}{\partial x_j \partial x_j} - \frac{\partial \tau_{ij}}{\partial x_j} \quad (3)$$

The influence of the smallest scales (the sub-grid scales) on the resolved velocities (\bar{u}_i) appears in the sub-grid stress tensor on the right side of Eq. 3, $\tau_{ij} = \overline{u_i u_j} - \bar{u}_i \bar{u}_j$. To model this term the Standard Smagorinsky model [15, 16] is used in the present work:

$$\tau_{ij} = -2\nu_{sgs} \bar{S}_{ij} \quad (4)$$

$\nu_{sgs} = (C_s f \Delta)^2 |\bar{S}|$ is the SGS viscosity and Δ is taken to be $\Delta = (\Delta_x \Delta_y \Delta_z)$ in the present work, where Δ_i are the local computational cell sizes in the three coordinate directions.

$$\bar{S}_{ij} = \frac{1}{2} \left(\frac{\partial \bar{u}_i}{\partial x_j} + \frac{\partial \bar{u}_j}{\partial x_i} \right) \quad (5)$$

is the resolved rate-of-strain tensor and $|\bar{S}| = (2\bar{S}_{ij}\bar{S}_{ij})^{\frac{1}{2}}$ is the magnitude of the rate-of-strain tensor. The value of the Smagorinsky constant $C_s = 0.1$ previously used in studies of similar types of unsteady flows around simplified trains and bluff bodies ([12, 13, 17]) is used in the present work. f in the expression for the SGS viscosity is the van Driest damping function

$$f = 1 - \exp\left(-\frac{n^+}{25}\right) \quad (6)$$

where n^+ is the wall normal distance in viscous units.

3.2 Numerical method

Equations (2) and (3) are discretized using a commercial finite volume solver, AVL Fire v2010.1 ([18]). The discretization is done using a collocated grid arrangement.

The convective fluxes are approximated by a blend of 95% linear interpolation of second order accuracy (central differencing scheme) and of 5% upwind differences of first order accuracy (upwind scheme). The time marching procedure is done using the implicit second-order accurate three-time level scheme:

$$\left(\frac{d\phi}{dt}\right)_n = \frac{3\phi^n - 4\phi^{n-1} + \phi^{n-2}}{2\Delta t_n}, \Delta t_n = t - t_{n-1} = t_{n-1} - t_{n-2} \quad (7)$$

where indices "n" and "n-1" denote the new and old time levels, respectively. To determine the pressure, the discrete form of the filtered continuity equation (Eq. 2) is converted into an equation for the pressure correction which is solved by using the SIMPLE algorithm ([19]).

3.3 Computational grid

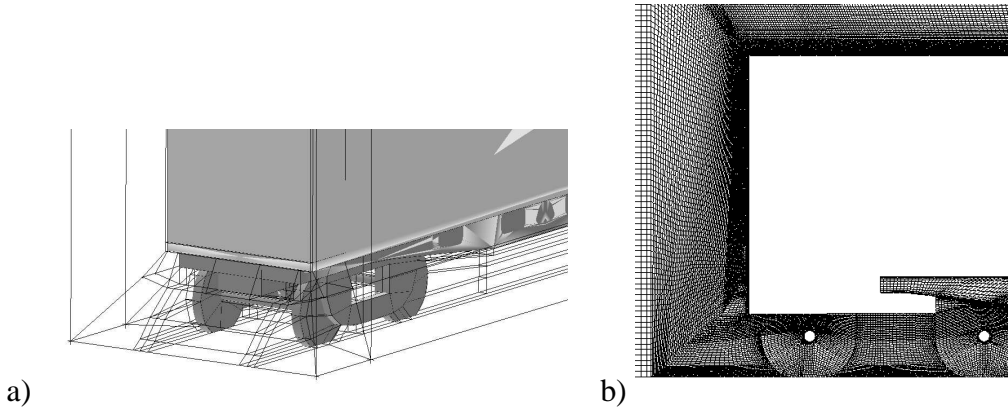


Figure 4: a) The blocking structure around the wheels and the front of the wagon used to construct the computational grid. b) A cut of the grid at $y = 0$.

One computational grid containing 17 million cells is used in the present work. The grid is block structured and was constructed using the grid generator software Ansys ICEM CFD. The grid consists of only hexahedral elements. In Fig. 4a the blocking structure around the front of the wagon is shown. The whole wagon is enclosed in an O-type blocking structure and the rest of the domain consists of H-type blocks. A considerable number of cells (80) in the normal direction of the O-type blocks is needed to resolve the geometrical details of the undercarriage of the wagon. 55% of the total number of cells in the grid is enclosed in the O-grid around the wagon. The blocking structure around the wagon is symmetric with respect to the y-z plane and the x-z plane (the geometry of the wagon is symmetric with respect to these planes as well). The distribution of cells is however not symmetric in the x-z plane as more cells are located behind the wagon than in front of it in order to resolve the flow structures in the wake accurately. The grid is shown in Fig. 4b around the front of the wagon and undercarriage in a cut placed at $y = 0$. In Fig. 5 the grid on the surface of the wagon

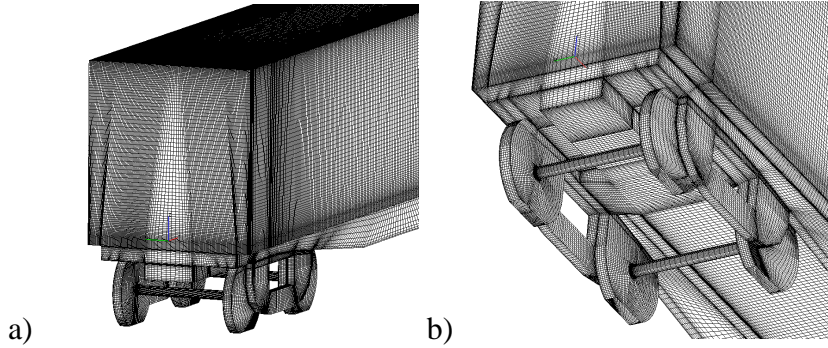


Figure 5: Two figures showing the computational grid on the surface of the wagon.

is shown. Hyperbolic stretching of the grid is used in order to concentrate grid points near the walls. Thus, the sizes of the cells are non-uniformly distributed and the cells might also be skewed.

3.4 Computational domain and boundary conditions

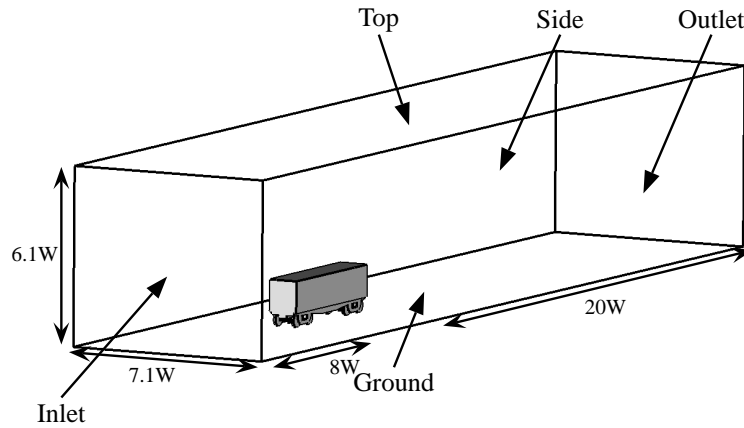


Figure 6: The computational domain around the wagon and the boundary conditions.

The computational domain is presented in Fig. 6. The cross sectional area is $7.1W \times 6.1W$ giving a blockage area in the numerical wind tunnel of 3.7%. From the inlet to the front of the wagon the distance is $8W$. From the aft of the wagon to the outlet the distance is $20W$. These distances are standard distances used in studies mentioned in the introduction of similar types of vehicle bluff body flows. On the inlet a uniform and constant in time velocity profile of $U_\infty = 1.1$ m/s was used. This corresponds to a Reynolds number of 100 000 based on the width of the wagon, inlet velocity U_∞ and the kinematic viscosity of air at temperature 20°C , $\nu = 1.5 \times 10^{-5}$ m^2/s . On the lateral sides and top of the domain a symmetry condition was used ($\partial\bar{u}/\partial y = \partial\bar{w}/\partial y = \bar{v} = 0$ on the sides and $\partial\bar{u}/\partial z = \partial\bar{v}/\partial z = \bar{w} = 0$ on the top).

On the outlet the homogenous Neumann condition was used ($\partial \bar{u}_i / \partial x_i = 0$). On the ground the no-slip condition was used in conjunction with setting the velocity component in the stream wise direction equal to the free streaming velocity ($\bar{u} = U_\infty, \bar{v} = 0$ and $\bar{w} = 0$). This is done in order to accurately simulate the effects on the flow due to the movement of the wagon over ground [20].

4 Evaluation of numerical accuracy: temporal and spatial resolution

The flow field was averaged during 100 000 time steps. This corresponds to 45 convective time units $t^* = tU_\infty/L$ (L is the length of the wagon). The size of the time step in physical time was 0.0015 s and in convective time units $\Delta t^* = \Delta tU_\infty/L = 0.00013$. This timestep kept the CFL number below one in more than 99% of the cells all the time. It was only exceeding one in a very small volume fraction of cells near the front edges on the wagon.

The idea behind a successful LES simulation employing a explicit model for the sub-grid terms as in the present work is to use a computational grid that is fine enough to resolve all the motion down to the inertial subrange [16]. After a LES simulation the obtained spatial resolution must be evaluated in order to assess the quality of the obtained results. In attached boundary layer flows the size of the grid cells close to the wall must be small enough to resolve the low and high speed streaky structures in the viscous region of the boundary layer ($y^+ < 10$). $y^+ = \Delta y / \lambda^+$ is the wall-normal distance measured in the viscous length unit $\lambda^+ = \nu / u^*$ where u^* is the wall friction velocity. The guidelines in the literature say that the size of the cells adjacent to the wall should be $\Delta n = 2 \lambda^+, \Delta x = 100 \lambda^+$ and $\Delta s = 20 - 30 \lambda^+$ in order to resolve the streaky structures [21]. Δn is the size of the cell in the normal direction. Δx is the size of the cell in the streamwise direction. Δs is the size of the cell in the spanwise direction. The mean spanwise spacing between low-speed streaks is reported from experimental studies to be around $100-120 \lambda^+$ and the spanwise width of the low-speed streaks is reported to range from $33-100 \lambda^+$. The mean length of the streaks are reported to be around $1000 \lambda^+$ but much shorter and longer lengths can be observed ([22, 23, 24]. In Fig. 11 low and high speed streaky structures in the viscous layer are shown from the experimental study [24]. For a comprehensive review and description of streaks and other coherent flow structures occurring in the turbulent boundary layer and the present understanding of them we refer the reader to [25].

In other flow situation such as separated flow, there exist no general guidelines of how the resolution in the simulation can be evaluated [26]. In scientific studies where LES is used some flow properties (e.g. forces, velocity profiles, Reynolds stress profiles, pressure distribution) are normally compared to experimental wind tunnel data in order to assess the quality of the results from the simulation.

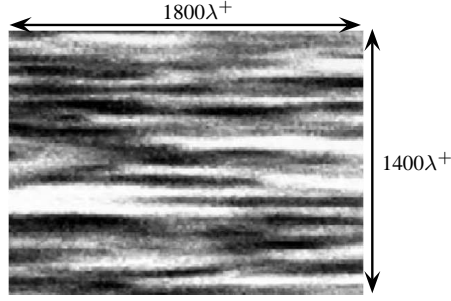


Figure 7: Thermal image from the experimental study of spatial characteristics of near-wall streaks in boundary layers. Picture is taken from [24]. Dark regions corresponds to high-velocity regions and bright regions are low-velocity regions.

The present work is a purely numerical investigation. In order to show that the employed computational grid provided a sufficiently fine spatial resolution in the simulation the resolution is calculated after the simulation. On the whole wagon, the obtained time-averaged resolution in the normal direction gives that the first grid points are located within $0 < \lambda_t^+ < 2$ on the wagon. The subscript t refers to the time-averaged value. The spatial mean of λ_t^+ on the wagon is 0.5. The values are somewhat higher on the wagon around the undercarriage details. On the side and roof of the container a boundary layer is formed after the initial separation (See Fig. 14 in Section 5). The largest cell size in spanwise direction of the grid is $\Delta s = 12.5\lambda_t^+$ and in streamwise direction $\Delta x = 30\lambda_t^+$.

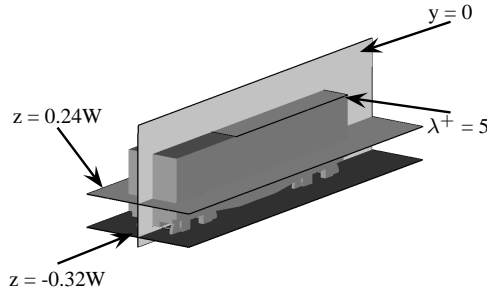


Figure 8: Planes that are used to plot time-averaged streamlines to visualise the flow around the wagon.

One cut showing the instantaneous streamwise velocity component at approximately $\Delta n = 5\lambda^+$ from the wall on the second half of the roof is presented in Fig. 9. Streaky structures of low (white regions) and high (dark regions) speed can be identified on the right part of the plane. The location of the plane is indicated in Fig. 8. The white areas of low speed fluid on the left part are due to the separated flow on the front of the roof. The value of the calculated mean viscous length λ_t^+ on the second half of the roof where the flow is attached is 0.0016.

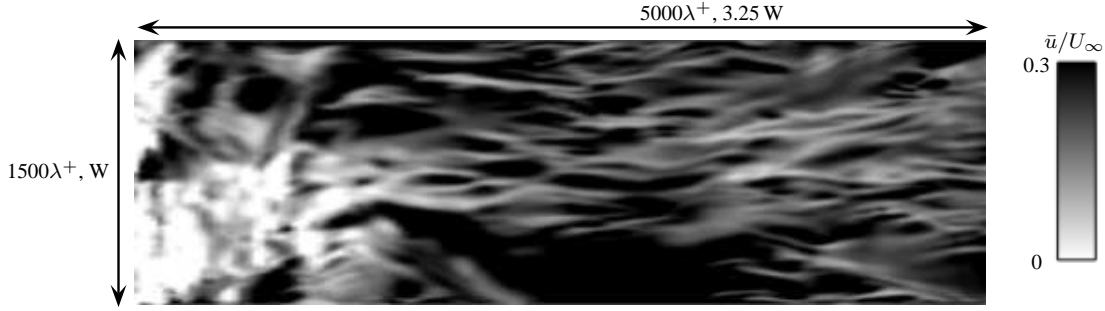


Figure 9: A plane showing the instantaneous velocity component \bar{u} on the roof. The cut is taken at a distance of approximately $5\lambda^+$ from the wall. Dark regions corresponds to high-velocity regions and bright regions are low-velocity regions.

5 Results

In this section the results from the simulation are presented. First the global quantities and then the time-averaged flow field around the wagon are presented.

5.1 Global quantities

Table 1: Aerodynamic forces on the container wagon from the simulation. See text for definition of the force coefficients.

Aerodynamic coefficients	C_D	$rms(C_D)$	C_S	$rms(C_S)$	C_L	$rms(C_L)$
Whole wagon	0.90	0.013	-0.0006	0.047	-0.05	0.029
Container	0.67	-	-	-	-	-
Undercarriage	0.23	-	-	-	-	-

The time-averaged forces from the simulation are presented in Table 1. The aerodynamic coefficients are defined as follows:

$$F_x = \frac{1}{2}C_D\rho U_\infty^2 A_x ; F_y = \frac{1}{2}C_S\rho U_\infty^2 A_x ; F_z = \frac{1}{2}C_L\rho U_\infty^2 A_x \quad (8)$$

$\rho = 1.18 \text{ kg/m}^3$ is the constant density of air at 20°C . U_∞ is the free stream velocity of the air and $A_x = 1W \times 1.6W$ is the cross-sectional area of the freight wagon projected onto the $y - z$ plane. Thus, the same cross-sectional area is used to normalize all three force components. The time-averaged value of the drag coefficient is 0.90. 74% of the drag comes from the container and the rest comes from the undercarriage details. The obtained drag coefficient can be compared to the value of the drag coefficient reported in other studies. For a similar type of wagon but with a more smooth undercarriage a drag coefficient around 0.8 for a Reynolds number of 10^6 is reported in Ref. [27]. In Ref. [28] drag coefficients of around 0.9 are reported for

Reynolds numbers based on length ranging from 5×10^6 to 30×10^6 for wind tunnel measurements on a single, 1:3 scale geometrically detailed container wagon model. Splitting up the contribution to the drag force in the present simulation into the friction part and the pressure part of the fluid force exerted on the wagon shows that only 3% of the total drag on the wagon can be attributed to the fluid friction force of the drag. This is due to the areas of separated flow around the front of the wagon as will be seen in the figures showing the flow field in the next subsection. The time-averaged side force is very close to zero ($C_S = -0.0006$) which indicates that the flow field has been averaged during a sufficiently long time.

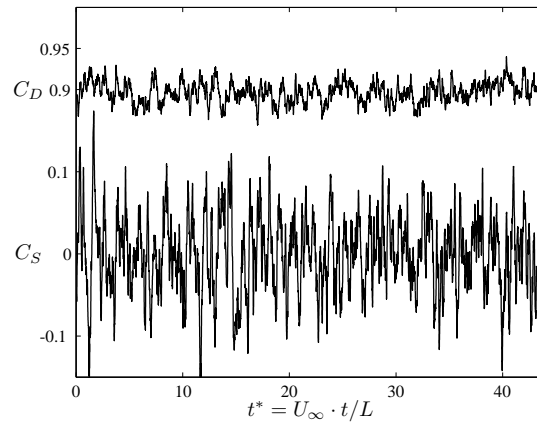


Figure 10: Time signals for drag and side force coefficients. L in the dimensionless time t^* is the length of the wagon.

In Fig. 10 the time histories of the drag of side forces are presented, respectively. The size of the oscillations in the drag is significantly smaller than the oscillations in the side force. The standard deviation of the former is 0.013 and for the latter it is 0.047. Power Spectral Densities (PSD) of the time signals of the drag and side forces are plotted in Fig. 11 versus the Strouhal number defined by $St = W \times f / U_\infty$ where f is the frequency. Three distinct peaks in the spectrum of the drag signal can be identified: $St = 0.07, 0.24$ and 0.5 . The peaks in the spectrum of the side force signal are: $St = 0.18, 0.26, 0.33, 0.55, 0.61, 0.72$ and 0.83 . Thus, the side force contain more high frequency peaks than the drag force.

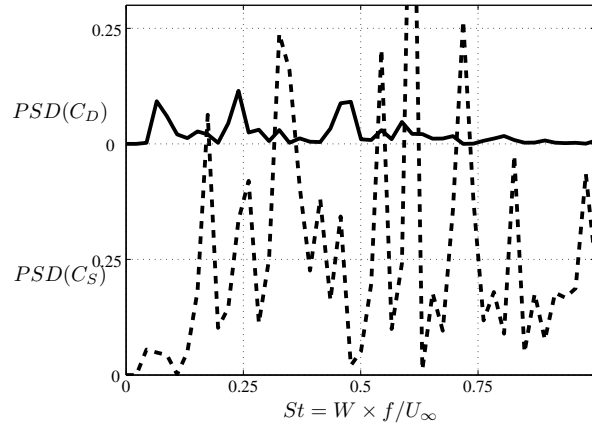


Figure 11: Power Spectral Density of the time signals for drag and side force coefficients.

5.2 Pressure distribution on the wagon

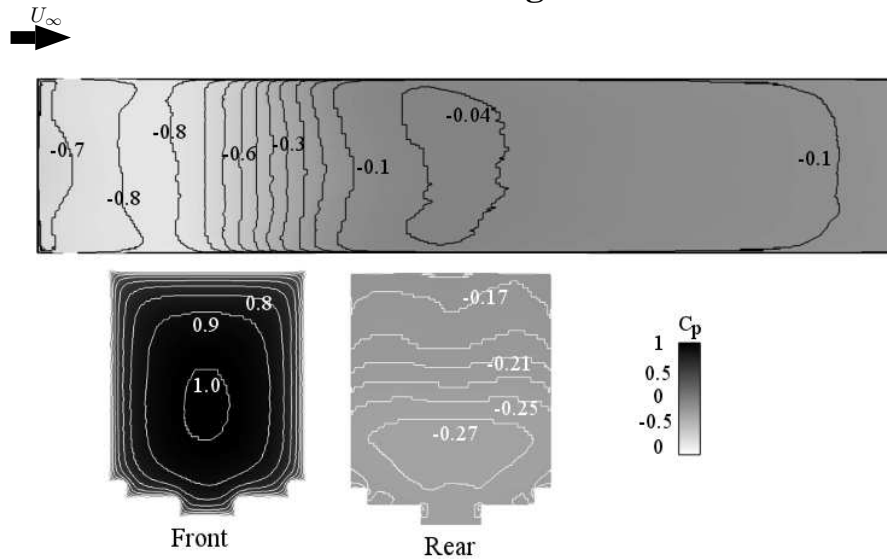


Figure 12: The pressure coefficient C_p on the roof (top), front and rear of the wagon, respectively.

In Fig. 12 the mean pressure coefficient defined as $C_p = (p_t - p_\infty)/0.5\rho U_\infty$ is shown on the roof, front and rear of the wagon, respectively. On the roof, low pressure in the region of the separated flow on the front can be observed. As the flow reattaches on the roof, the pressure increases. On the front the stagnation pressure can be observed. On the rear face the pressure is slightly negative and rather uniformly distributed.

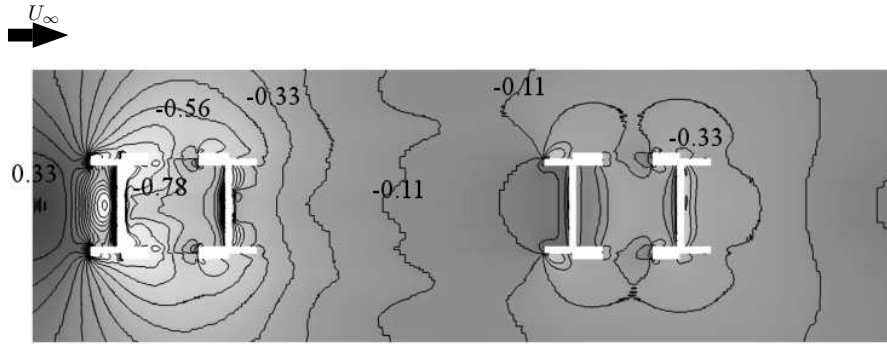


Figure 13: The pressure coefficient C_p in the plane $z = -0.32W$

The pressure in the undercarriage plane $z = -0.32W$ (see Fig. 8) is presented in Fig 13. Low pressure is observed around the front wheel part due to the separation from the front edge. The pressure increases further downstream but stays negative everywhere.

5.3 Time-averaged streamlines of the flow around the wagon

Three planes are used to visualise the flow by assistance of streamlines of the time averaged velocity around the wagon. The locations of these planes are shown in Fig. 8 in Section 4.

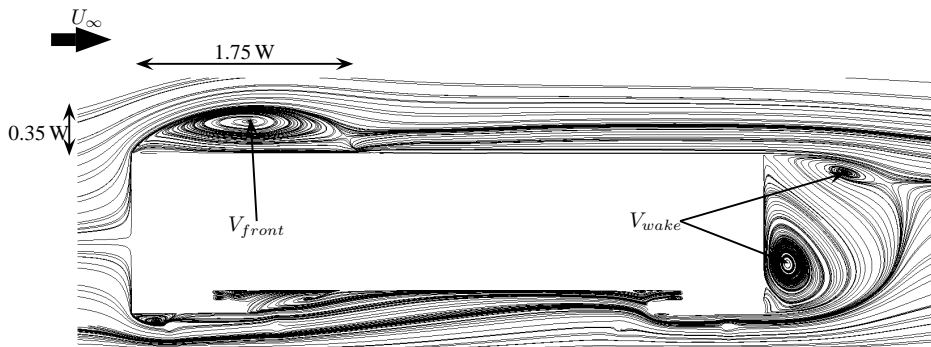


Figure 14: Streamlines of the time-averaged velocity field \bar{u}_t projected onto the plane $y = 0$.

In Fig. 14 streamlines of the time-averaged velocity projected onto the plane $y = 0$ are presented. The flow separates from the sharp edges on the front of the wagon and forms a separation bubble on the roof. This bubble is denoted V_{front} in Fig. 14. The extent in streamwise direction of V_{front} is $1.75W$ and the height is $0.35W$. After the separation from the front edge the flow re-attaches and a boundary layer develops along the roof of the wagon before the flow separates into the wake and forms the

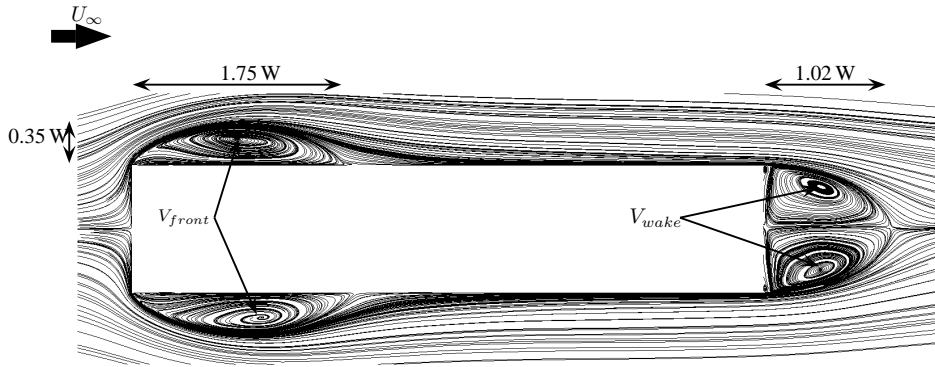


Figure 15: Streamlines of the time-averaged velocity field (\bar{u}_t) projected onto the plane $z = 0.24W$.

vortex in the wake denoted by V_{wake} in Fig. 14. Streamlines in the plane $z = 0.24W$

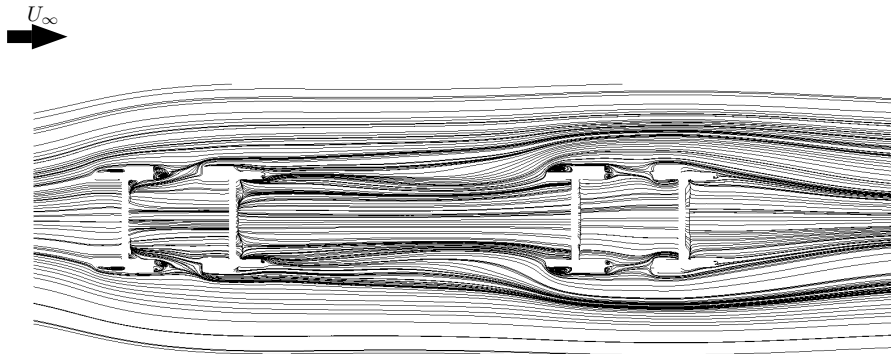


Figure 16: Streamlines of the sampled mean velocity field (\bar{u}) projected onto the plane $z = -0.32W$.

(see Fig. 8) are presented in Fig. 15. The separated flow forms a bubble on the sides of the same size as the bubble on the roof. After separation the flow re-attaches to the sides and then separates into the wake. The length of the wake vortex V_{wake} in the streamwise direction is $1.02W$. In Fig. 16 streamlines in the plane cutting the undercarriage $z = -0.32W$ are shown. The time-averaged flow is rather smooth in that plane.

6 Discussion

In Fig. 17 the vortex system around the wagon is shown. The black lines in the figure are vortex cores calculated in the visualisation software package EnSight. The method for vortex core identification is based on critical-point concepts for fluid flow (e.g [29]) and finds eigenvalues and eigenvectors to the rate-of-deformation tensor of

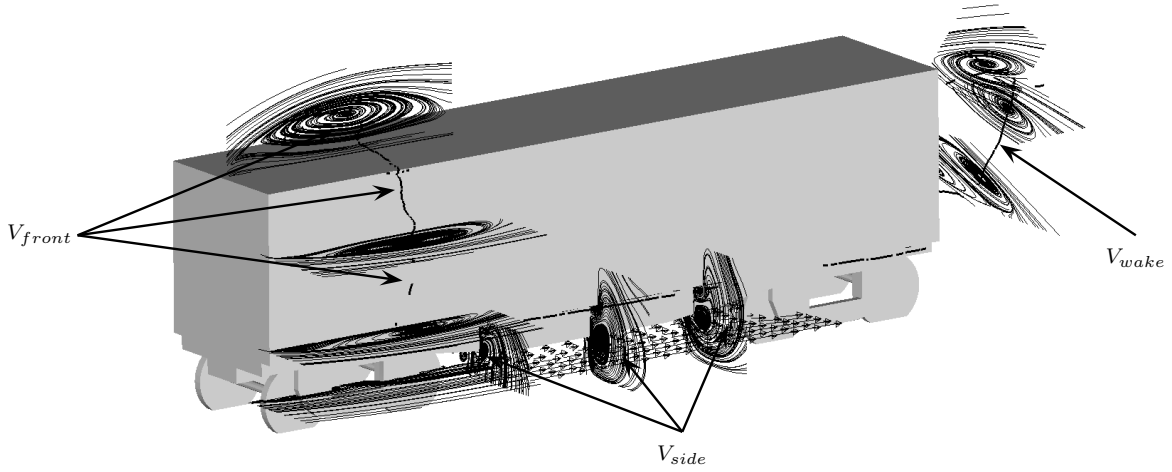


Figure 17: The mean flow around the wagon.

the filtered velocity, $\partial \bar{u}_i / \partial x_j$. A full description of the algorithm is given by [30]. The algorithm can produce non-existing cores and should only be used as a tool to help localize vortices ([30]). Streamlines around cores are used in the present work to assure that the cores really exist. The large separation bubble on the front part of the roof and sides is denoted V_{front} . It extends all the way around the front part and creates low pressure on the surface of the wagon as seen in the pressure distribution in Fig. 12. Along the side of the wagon a longitudinal vortex is formed. It is denoted V_{side} in Fig. 17. The strength of this vortex is however rather weak which can be seen on the arrows in Fig. 17 showing the direction of the flow and the time-averaged spanwise velocity around it in Fig. 18a. V_{side} emanates from flow being pushed to the sides under the wagon. This push of the flow outwards can be seen in the streamlines in the plane $z = -0.32$ in Fig. 16 as well.

In Fig. 18 streamlines are shown in a plane cutting the x-axis at $x = 2.5W$ under the wagon. Fig. 18a shows streamlines of the time-averaged velocity field and 18b and c show streamlines of the instantaneous velocity at one realization of the flow field each. The time between the realizations is $\Delta t^* = 0.5$. In the instantaneous flow field, there are many smaller vortices visible compared to the time-averaged flow field.

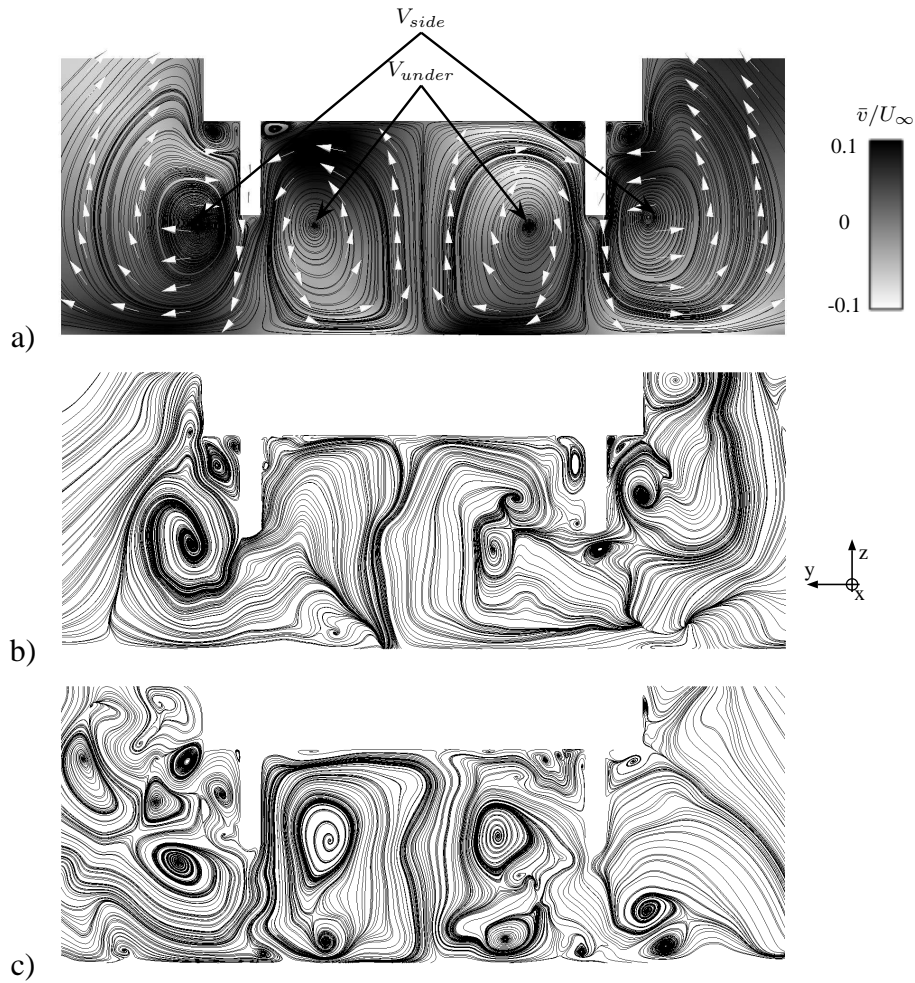


Figure 18: a) Streamlines of the time-averaged velocity in the plane $x = 2.5W$. The background in the figure is colored with the time-averaged span wise velocity \bar{v}_t . b) Instantaneous streamlines in the same plane at one realization. c) Instantaneous streamlines in the same plane.

7 Conclusion

In this work the flow around a single standing container freight wagon has been simulated successfully. The numerical technique that was used was LES. The container wagon model consisted of a 11.8 m long container placed on a 8 wheel freight-liner. The Reynolds number in the simulation was 10^5 based on the width of the container. The work was purely numerical and no direct comparisons to any wind tunnel experiments or other numerical studies could be done. However, the value of the drag coefficient (0.90) in the simulation correlated well with values from wind tunnel studies where similar types of container freight wagons were studied. The side force signal was found to contain larger oscillations and a broader spectrum of frequencies compared to that of the drag force signal. 74% of the drag force was found to come from the container. The rest comes from the undercarriage. The calculated spatial reso-

lution in the simulation showed that the resolution was very fine even compared to standard requirements for well-resolved LES simulations. Visualization of the flow field with the help of streamlines showed that the flow around the front of the wagon is governed by a large separation originating from the leading edges. The flow under the wagon is more complex.

Acknowledgements

This project is supported financially by Trafikverket (Swedish Transport Administration). Software licenses were provided by AVL List GMBH. Computations were performed at SNIC (Swedish National Infrastructure for Computing) at the Center for Scientific Computing at Chalmers (C3SE), Center for High Performance Computing at KTH (PDC) and National Supercomputer Center (NSC) at LiU.

References

- [1] W.J. Jr. Davis. The tractive resistance of electric locomotives and cars. *Gen. Electr. Rev.*, 29:2–24, 1926.
- [2] Raghu S. Raghunathan, H.-D. Kim, and T. Setoguchi. Aerodynamics of high-speed railway train. *Progress in Aerospace Sciences*, 38:469–514, 2002.
- [3] B. P. Rochard and F. Schmid. A review of methods to measure and calculate train resistances. *Proc. IMechE, Part F: Journal of Rail and Rapid Transit*, 214:185–199, 2000.
- [4] P. Lukaszewicz. *Energy Consumption and Running Time for Trains*. PhD thesis, Royal Institute of Technology, 2001.
- [5] P. Lukaszewicz. Running resistance - results and analysis of full-scale tests with passenger and freight trains in sweden. *Proc. IMechE, Part F: Journal of Rail and Rapid Transit*, 221:183–193, 2006.
- [6] R. Engdahl. Full-scale rail car testing to determine the effect of position-in-train on aerodynamic resistance. In *Publication R-705*. Association of American Railroads, 1987.
- [7] S. Watkins, J.W. Saunders, and H. Kumar. Aerodynamic drag reduction of goods trains. *Journal of Wind Engineering and Industrial Aerodynamics*, 40:147–78, 1992.
- [8] J.W. Saunders, S. Watkins, and R.J. Cassar. Vortex optimisation of slotted tops and cavities of two different open rail wagons. *Journal of Wind Engineering and Industrial Aerodynamics*, 49:421–430, 1993.

- [9] F. Alam and S. Watkins. Lateral stability of a double stacked container wagon under crosswinds. In *Proceedings of the International Conference on Mechanical Engineering 2007 (ICME2007)*, pages 225–242, Dhaka, Bangladesh, 2007.
- [10] H. Hemida and C. Baker. Large-eddy simulation of the flow around a freight wagon subjected to a crosswind. *Computers & Fluids*, 39:1944–1956, 2010.
- [11] H. Hemida, S. Krajnović, and L. Davidson. Large eddy simulations of the flow around a simplified high speed train under the influence of cross-wind. In *17th AIAA Computational Dynamics Conference*, Toronto, Ontario, Canada, 2005.
- [12] H. Hemida and S. Krajnović. Les study of the influence of a train-nose shape on the flow structures under cross-wind conditions. *ASME: Journal of Fluids Engineering*, 125:091101–1–12, 2008.
- [13] H. Hemida and S. Krajnović. Les study of the influence of the nose shape and yaw angles on flow structures around trains. *Journal of Wind Engineering and Industrial Aerodynamics*, 98:34–46, 2010.
- [14] H. Hemida, N. Gil, and C. Baker. Les study of the slipstream of a rotating train. *ASME: Journal of Fluids Engineering*, 132:051103–1–9, 2010.
- [15] J. Smagorinsky. General circulation experiments with the primitive equations. *Monthly Weather Review*, 91(3):99–165, 1963.
- [16] S. B. Pope. *Turbulent Flows*. Cambridge University Press, Cambridge, first edition, 2000.
- [17] S. Krajnović. LES of flows around ground vehicles and other bluff bodies. *Philosophical Transactions of the Royal Society A*, 367(1899):2917–2930, 2009.
- [18] AVL, 2010. CFD Solver. AVL Fire Manual, v2010.1, edition 11/2010.
- [19] S.V. Patankar and D.B. Spalding. A calculation procedure for heat, mass and momentum transfer in three-dimensional parabolic flows. *Int. J. Heat Mass Transfer*, 15:1787–1806, 1972.
- [20] S. Krajnovic and L. Davidson. Influence of floor motions in wind tunnels on the aerodynamics of road vehicles. *Journal of Wind Engineering and Industrial Aerodynamics*, 93:677–696, 2005.
- [21] L Davidson. Large eddy simulations: How to evaluate resolution. *International Journal of Heat and Fluid Flow*, 30(5):1016 – 1025, 2009.
- [22] S. J. Kline, W. C. Reynolds, F. A. Schraub, and Rundstadler P. W. The structure of the turbulent boundary layer. *Journal of Fluid Mechanics*, 30:741–773, 1967.

- [23] C. R. Smith and S. P. Metzler. The characteristics of low-speed streaks in the near-wall region of a turbulent boundary layer. *Journal of Fluid Mechanics*, 129:27–54, 1983.
- [24] M. Zacksenhause, G. Abramovich, and G. Hetstoni. Automatic spatial characterization of low-speed streaks from thermal images. *Experiments in Fluids*, 31:229–239, 2001.
- [25] R. J. Adrian. Hairpin vortex organization in wall turbulence. *Physics of Fluids*, 19:041301, 2007.
- [26] L Davidson. How to estimate the resolution of an les of recirculating flow. *Quality and Reliability of Large-Eddy Simulations II*, 16(5):269–286, 2010.
- [27] A. G. Hammit. Aerodynamic forces on freight trains: Volume 1 - wind tunnel tests of containers and trailers on flatcars. In *Report No. FRA/ORD-76-295.I*. U.S. Department of Transportation, 1976.
- [28] J. L. Peters. Effect of reynolds number on the aerodynamic forces on a container model. *Journal of Wind Engineering and Industrial Aerodynamics*, 49:431–438, 1993.
- [29] A. E. Perry and M. S. Chong. A description of eddy motions and flow patterns using critical-point concepts. *Ann. Rev. Fluid Mech.*, 19:125 – 155, 1987.
- [30] D. Sujudi and R. Haines. Identification of swirling flow in 3-d vector fields. AIAA Paper 95-1715, 1995.